Journal of Materials Chemistry A

ROYAL SOCIETY OF CHEMISTRY

PAPER

View Article Online
View Journal

Cite this: DOI: 10.1039/d6ta00156d

New MXene-derived anthracene-based metal–organic framework with controllable morphology for high-performance sensing

Nasrin Kabeer,†[a] Mostafa Zeama,†[a] Yusuf khan,[b] Hadeer Elsayed,[b] Jehad K. El-Demellawi,[b] Anita Justin,[a] Vinayak S. Kale,[a] Osama Shekhah,[a] Omar F. Mohammed,[b] Husam N. Alshareef *[bc] and Mohamed Eddaoudi *[a]

Morphological variations in metal–organic frameworks (MOFs), such as differences in shape and size, critically influence their properties, including surface area, mechanical strength, and optical behaviour. These morphological features are often controlled by synthetic parameters, thereby directly affecting MOF performance in applications such as catalysis and sensing. In this study, we present a novel approach in which MXenes are used as a metal precursor to synthesize MOFs with ultrathin two-dimensional (2D) nanosheet morphologies, offering promising potential for device integration. Specifically, we synthesized an anthracene-based vanadium MOF (V–A MOF) with two distinct morphologies: bulk nanorods derived from $VOSO_4$ as the metal precursor ($VOSO_4$–A MOF) and ultrathin nanosheets derived from V_2C MXene as the metal precursor (V_2CT_x–A MOF). The combination of π-conjugated anthracene ligands and redox-active vanadium centers yields strong fluorescence emission. Structural analyses confirmed successful synthesis and morphology control. Both MOFs were evaluated as optical sensors for detecting metal ions and nitroaromatic compounds. Photoluminescence studies revealed highly sensitive and selective fluorescence quenching toward Fe^{3+} and Pb^{2+} ions, with the V_2CT_x–A MOF nanosheets demonstrating up to a sixfold enhanced response compared with that of the bulk nanorods. Mechanistic investigations, supported by spectroscopic techniques and density functional theory (DFT) calculations, indicate that fluorescence arises from linker-to-metal charge transfer, whereas sensing predominantly occurs *via* Förster resonance energy transfer. This work highlights the profound impact of the framework structure and nanoscale morphology on the accessibility of active sites and overall sensing efficiency, emphasizing the advantages of MXene-derived nanosheets in enhancing MOF-based sensor performance.

Received 7th January 2026
Accepted 9th April 2026

DOI: 10.1039/d6ta00156d

rsc.li/materials-a

Introduction

While the reticular chemistry of metal–organic frameworks (MOFs) has achieved remarkable precision in tuning pore topology, the extrinsic control of crystal morphology, from bulk polyhedra to ultrathin nanosheets, remains a critical frontier in maximizing mass transport and active site accessibility for advanced sensing applications.[1–4] There has been a surge in recent studies on MOFs focused on developing techniques to achieve different morphologies, understand the origins of morphological variation, tune the shape and size of crystallites in a controllable manner, and investigate their effects on functional properties.[5–11]

MOFs are emerging as powerful platforms for different sensing applications, especially fluorescence-based sensors.[12–17] The topology of a MOF, defined by the connectivity of its metal clusters and organic linkers, dictates the pore geometry, linker distribution, and overall accessibility of guest molecules, whereas the diffusion dynamics and surface exposure of active sites are governed by the morphology (*e.g.*, bulk crystals *vs.* nanosheets).[18] Rational control over these parameters can significantly enhance sensor performance by improving analyte accessibility and optimizing host–guest interactions.[19] Vanadium (V) is a transition metal belonging to the fifth group of the periodic table and possesses an outer electronic configuration of $3d^3 4s^2$. This configuration provides multiple valence electrons, allowing vanadium to exhibit a wide range of oxidation

[a]*Functional Materials Design, Discovery and Development Research Group (FMD3), Division of Physical Science and Engineering (PSE), King Abdullah University of Science and Technology (KAUST), Thuwal 23955-6900, Kingdom of Saudi Arabia. E-mail: mohamed.eddaoudi@kaust.edu.sa*

[b]*Center for Renewable Energy and Storage Technologies (CREST), King Abdullah University of Science and Technology, Thuwal, 23955-6900, Saudi Arabia. E-mail: Husam.alshareef@kaust.edu.sa*

[c]*Materials Science and Engineering, Physical Science and Engineering Division, King Abdullah University of Science and Technology (KAUST), Thuwal, 23955-6900, Saudi Arabia*

† N. K. and M. Z. contributed equally to this work.

states and redox activity. As a result, vanadium-based compounds including vanadium oxides, nitrides, sulfides, mixed-metal vanadates, and vanadyl phosphates have attracted increasing attention for applications in electrochemical energy conversion and storage, as well as in sensing technologies.[20–22]

In recent years, vanadium-based MOFs (V-MOFs) have emerged as promising materials because they provide new opportunities for constructing functional vanadium-containing architectures. In addition to incorporating vanadium into well-defined frameworks, these materials can exhibit advantageous properties such as high surface area, tunable porosity, structural diversity, and good chemical stability. V-MOFs are typically formed through the coordination-driven self-assembly of vanadium ions with organic ligands, leading to extended network structures. Commonly used vanadium precursors include vanadium trichloride (VCl_3), vanadyl sulfate ($VOSO_4$), and elemental vanadium powder. These metal sources generally coordinate with multidentate carboxylate ligands or nitrogen-containing heterocyclic linkers to generate three-dimensional frameworks with diverse structural topologies.[8–10] Several synthetic approaches have been explored to prepare V-MOFs with controlled morphologies, including hydrothermal or solvothermal synthesis, ultrasonic-assisted methods, and coprecipitation techniques. Despite these developments, the number of well-characterized crystalline V-MOFs reported in the literature for sensing applications remains relatively small.[20–24] For example, porphyrinic V-MOF-10 has dual-pore systems, a large surface area, and visible-light absorption properties favorable for optical sensing.[21,25] Similarly, polyoxovanadate-based MOFs (POV-MOFs) incorporate vanadium–oxygen clusters as nodes, enhancing framework stability, redox activity, and linker accessibility.[22,25,26]

On the other hand, MXenes, a rapidly expanding class of two-dimensional (2D) materials, have shown exceptional properties.[27,28] MXenes have attracted significant attention due to their exceptional, uniquely tunable features, which are related to their adaptable surface chemistry. In energy and environmental applications, MXenes have demonstrated significant promise.[29–31] MXenes are generally obtained by selectively etching A-site layers from their parent MAX phases, followed by chemical etching. The 2D layered structure of MXenes follows the generic formula $M_{n+1}X_nT_x$, where T_x denotes surface functional groups, including –O, –OH, –F, and –Cl.[27,28] Using V_2CT_x MXene as a sacrificial metal precursor, Wu *et al.* (2019) successfully demonstrated the synthesis of precisely thickness-controlled vanadium porphyrin framework (V-PMOF) nanosheets by coordinating deprotonated tetrakis(4-carboxyphenyl) porphyrin (H_4-TCPP) ligands.[32] This discovery revealed a successful method for building MOF structures with controlled morphologies directly from MXenes. The use of MXenes as sacrificial metal precursors in this system is driven by their distinctive structural and chemical properties. Unlike their parent MAX phases, MXenes exhibit a two-dimensional layered morphology and are enriched with surface termination groups such as –O, –OH, and –F that are introduced during the etching process. These surface functionalities serve as active coordination sites for metal ions and organic ligands, thereby promoting the nucleation and growth of MOF structures. Furthermore, the large surface area, strong hydrophilicity, and high chemical reactivity of MXenes make them highly suitable as templates or precursors for MOF formation. During the synthesis process, the two-dimensional MXene sheets can participate in coordination interactions, enabling the *in situ* formation of MOFs with two-dimensional architectures or well-controlled morphologies. This strategy can also facilitate a more uniform distribution of active sites and enhance their accessibility, which is advantageous for sensing-related applications. Nevertheless, the synthesis of MOFs from MXenes and their applications across various domains remain largely unexplored.[32]

Heavy metal contamination, particularly from Fe^{3+} ions such as micronutrients involved in enzymatic catalysis and oxygen transport, can induce oxidative stress and organ dysfunction.[33,34] In contrast, Pb^{2+} has no biological role and is highly toxic even at trace concentrations, leading to neurotoxicity, developmental impairments, and cardiovascular disorders.[35–37] Therefore, monitoring Fe^{3+} and Pb^{2+} in environmental, food, and biological samples is critically important. Conventional detection techniques, such as atomic absorption spectroscopy (AAS), inductively coupled plasma-mass spectrometry (ICP-MS), and inductively coupled plasma optical emission spectroscopy (ICP-OES), remain the analytical gold standards owing to their accuracy and sensitivity. AAS is cost-effective and simple but limited in terms of multielement analysis and ultratrace detection; ICP-MS provides exceptional sensitivity and isotopic resolution; and ICP-OES allows simultaneous multielement quantification across wide concentration ranges.[38,39] However, these methods require costly instrumentation, trained personnel, and laboratory-bound operations, emphasizing the need for portable, rapid, and low-cost detection alternatives.

Optical sensors, especially fluorescence-based sensors, are particularly attractive because of their high signal-to-noise ratios and design flexibility. Anthracene derivatives, in particular, are widely explored as fluorescent probes owing to their strong emission intensity, high photostability, and facile functionalization. For example, anthracene–quinoline dual-mode chemosensors (*e.g.*, HAQ) exhibit selective fluorescence quenching and visible color changes upon Fe^{3+} binding with low detection limits; anthracene–chalcone derivatives show strong Pb^{2+} selectivity *via* photoinduced electron transfer (PET) mechanisms; and multianthracene systems achieve sub-micromolar Fe^{3+} detection in environmental samples.[40,41] In a similar way, nitroaromatic compounds, including nitrobenzene, 2,4-dinitrotoluene (DNT), and 2,4,6-trinitrotoluene (TNT), are widely utilized in the production of explosives, industrial chemicals, and military materials. Despite their widespread use, these compounds pose significant environmental and health concerns due to their high toxicity, chemical stability, and potential security threats. Therefore, the development of sensitive and selective methods for their detection has become increasingly important. MOFs have attracted considerable attention as promising sensing materials for nitroaromatic compounds. Owing to their porous structures and tunable chemical functionality, MOFs can effectively interact with target

molecules. Consequently, luminescent MOFs have been widely explored as effective platforms for the rapid, sensitive, and portable detection of nitroaromatic pollutants and explosive residues.[5–8,42]

In a related study, two anthracene-functionalized zirconium-based MOFs were reported as luminescent sensors capable of selectively detecting Fe^{3+}, 2-nitrophenol, and dichromate ($Cr_2O_7^{2-}$), underscoring the potential of anthracene-based MOFs for multifunctional sensing applications.[42] Building on this concept, the present work focuses on integrating anthracene moieties into V-MOFs to couple the optical advantages of anthracene with the redox versatility of vanadium. Anthracene moieties act as efficient organic fluorophores, contributing strong π–π* transitions that significantly increase the fluorescence intensity and improve the sensitivity of the detection signal. In addition, these organic units can promote energy transfer processes between the vanadium nodes and the ligand framework, which may further improve the emission efficiency and produce clearer fluorescence signals. Beyond their photophysical contribution, anthracene derivatives also play an important structural role within the framework. As organic linkers, they help define the pore architecture and maintain the structural integrity of the MOF, thereby facilitating better accessibility of analyte molecules to the active sites while reducing nonradiative quenching pathways. Here, we report the synthesis of anthracene-based vanadium MOFs (V–A MOFs) with tunable morphologies to investigate their performance as optical sensors. Anthracene derivatives were used as organic linkers, whereas vanadium sulfate ($VOSO_4$) served as the metal precursor. To achieve morphological control, vanadium MXene (V_2CT_x) was employed as a metal precursor for constructing two-dimensional (2D) nanosheet MOFs, whereas the use of $VOSO_4$ yielded bulk crystalline V-MOFs (Fig. 1a). Comparative studies between these two morphologies elucidate how framework dimensionality, linker accessibility, and active-site distribution influence sensing efficiency. This approach not only deepens the understanding of morphology-driven sensing in V-MOFs but also pioneers the use of MXene-assisted templating as a versatile strategy for developing advanced optical sensors for heavy-metal detection.

Experimental section

Synthesis of MXene V_2CT_x from V_2AlC

The MXene was prepared according to previous reports.[43] 1 g of V_2AlC MAX phase powder was added to 20 mL of hydrofluoric acid (HF, 48% Sigma-Aldrich) to start the synthesis of V_2CT_x MXene. The resulting solution was gently agitated for 24 hours at 35 °C. After the etching procedure, the solution was centrifuged until a neutral pH was reached. The MXene dispersion was then delaminated by adding 10 mL of 1 M tetramethylammonium hydroxide (TMAOH) and stirring it for 4 hours at room temperature to facilitate effective intercalation and subsequent solvent-exchange with dimethylformamide (DMF).

Synthesis of the V_2CT_x–A MOF

The MXene-derived anthracene-based V_2CT_x–A MOF was synthesized through a solvothermal approach, where 20 mL

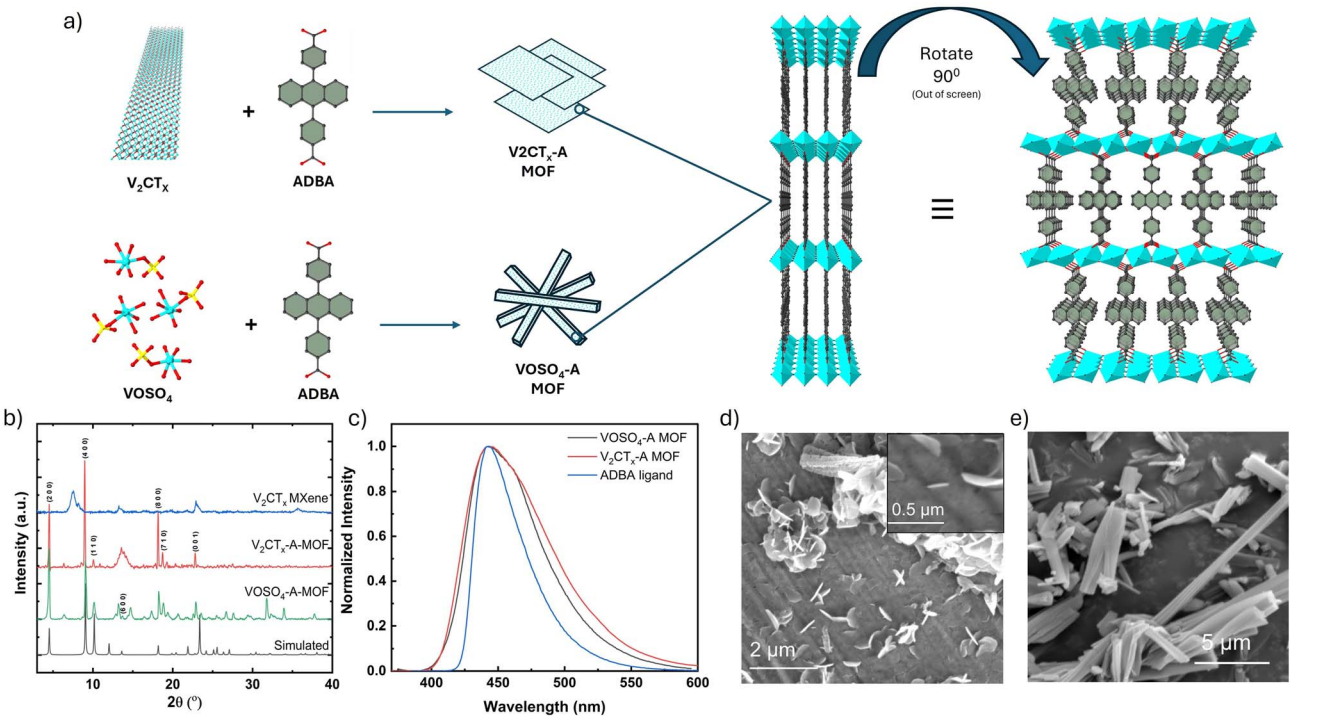

Fig. 1 (a) Synthesis scheme of the V-MOF. (b) PXRD patterns of the V_2CT_x–A MOF, $VOSO_4$–A MOF, V_2C MXene, and the simulated structure. (c) PL data for the V_2CT_x–A MOF, $VOSO_4$–A MOF, and the ADBA ligand. SEM images of the (d) V_2CT_x–A MOF and (e) $VOSO_4$–A MOF.

(1 mg mL^{-1}) of V_2CT_x MXene suspension in DMF was first sonicated for 5 minutes before 95 mg of the 4,4′-(anthracene-9,10-diyl)dibenzoic acid (ADBA) linker was gradually added to the mixture under continuous stirring. After 2 h of stirring, the solution was transferred into a 50 mL Teflon-lined autoclave. The reaction was carried out at 180 °C for 3 days. After 3 days of reaction, the mixture was allowed to cool naturally to room temperature. The product was washed thoroughly to remove unreacted species and residual solvent, and solvent exchange was performed with methanol for 24 h, followed by vacuum filtration at room temperature to obtain the final V_2CT_x–A MOF. Here after complete washing and solvent exchange we have obtained 26 mg of V_2CT_x–A MOF.

Synthesis of $VOSO_4$–A MOF

The synthesis of bulk $VOSO_4$–A MOF was carried out under conditions similar to those used for the synthesis of V_2CT_x–A MOF. In a typical procedure, 10 mg of $VOSO_4$ was dissolved in 20 mL of DMF under continuous stirring, followed by the gradual addition of 95 mg of the ADBA linker. The resulting light greenish precipitate was collected, thoroughly washed with DMF, and subjected to solvent exchange with methanol.

Results and discussion

In this work, we report, for the first time, the synthesis of a fluorescent bulk $VOSO_4$–A MOF and a V_2CT_x–A MOF, which were fully characterized and found to exhibit superior sensing capabilities.

Material characterization

The successful synthesis of V_2CT_x MXenes was first confirmed *via* PXRD analysis (Fig. 1b). The PXRD patterns of the parent V_2AlC MAX phase and the etched V_2CT_x MXene match well with standard reference data from the literature (Fig. S1a).[44] Transparent thin layers of V_2CT_x MXene are visible in the high-resolution SEM images (Fig. S1b and c). The shift and broadening of the (00*l*) reflections toward lower angles, along with the formation of thin 2D layers, confirm the successful etching and formation of few-layer MXenes.

This V_2CT_x MXene was subsequently employed as a metal precursor for the targeted MOF, while $VOSO_4$ was used under identical conditions to obtain the corresponding bulk MOF.

This V_2CT_x MXene was subsequently employed as a metal precursor for the targeted MOF, while $VOSO_4$ was used under identical conditions to obtain the corresponding bulk MOF. The PXRD patterns of both the $VOSO_4$–A MOF (bulk) and the V_2CT_x–A MOF (2D nanosheets) exhibit good agreement with the simulated pattern derived from a MIL-71-type structure, confirming the successful synthesis of the desired frameworks in both bulk and nanosheet morphologies. The diffraction pattern of the bulk $VOSO_4$–A MOF matches well with the expected crystalline phase, indicating the formation of a highly ordered structure.[45]

In contrast, the V_2CT_x–A MOF nanosheets display a distinct variation in relative peak intensities, particularly an enhanced contribution from the (200) crystallographic plane. This preferential exposure suggests anisotropic growth along specific crystallographic directions, leading to increased surface exposure of the anthracene-based ADBA linkers. Such a structural orientation is consistent with the formation of ultrathin 2D sheets and is expected to enhance analyte accessibility to the photoactive sites.

Notably, while the bulk precursor ($VOSO_4$) contains V^{4+} species, the resulting framework adopts a MIL-71-type structure composed of V^{3+} centers. This reduction is attributed to the solvothermal conditions, where DMF acts as a mild reducing agent at elevated temperatures, facilitating the conversion of VO^{2+} to V^{3+} during the formation of the metal–oxo clusters.

Le Bail fitting was performed using a structural model analogous to the MIL-71 framework with the same space group (Fig. S2). The fitted lattice parameters were determined to be $a = 39.209(8)$ Å, $b = 9.459(5)$ Å, and $c = 3.923(3)$ Å, which are in reasonable agreement with the previously reported values ($a = 38.9962$ Å, $b = 8.9178$ Å, and $c = 3.8020$ Å). The main diffraction peaks, including the (200), (400), (110), and (800) reflections, are well indexed based on this model, supporting the structural assignment.

A deviation is observed particularly along the *b*-axis (~0.55 Å), which is attributed to peak broadening and asymmetry, especially at higher diffraction angles, rather than the formation of a different crystalline phase. Additional broad features appearing at approximately 8° and 15° may arise from residual MXene stacking, indicating interlayer spacings characteristic of the precursor-derived morphology.[46]

Structurally, the V-MOF consists of corner-sharing vanadium(III) octahedra connected through oxygen atoms to form two-dimensional layers, which are pillared by the ADBA dicarboxylate linkers. This results in a chain-like framework topology similar to that of MIL-71, with the nanosheet morphology promoting enhanced exposure of the functional organic linkers at the surface.[46]

The FTIR spectra of both the V_2C–A MOF and the free ADBA ligand exhibited the characteristic vibrations of the organic linker (Fig. S3). The observed redshift of the bands in the MOF spectrum indicates the coordination of the ligand to the vanadium centers. The disappearance of the COOH stretching band at approximately 1700 cm^{-1} confirms the deprotonation and coordination of the carboxylate groups in the MOF framework. To evaluate the thermal stability, thermogravimetric analysis (TGA) was performed at a heating rate of 5 °C min^{-1} under N_2 flow up to 800 °C. The TGA curves (Fig. S4) show that both materials remain stable up to ~400 °C without significant mass loss, indicating excellent thermal stability. Beyond this temperature, MXenes retain nearly 80% of their initial mass at 800 °C, matching the calculated V content in the MOF. A comparison of the TGA profiles further demonstrated that the synthesized MOF and pristine MXenes exhibited distinct stability behaviors.

The porosities of the V_2CT_x–A MOF and $VOSO_4$–A MOF were assessed *via* N_2 sorption isotherms, both of which were type-I isotherms, which are typical of microporous materials (Fig. S5 and S6). The porosity is assessed *via* N_2@77 K, and the material

exhibits a type 1 isotherm with an estimated surface area of 354 $m^2\ g^{-1}$ and pore volume of 0.15 $cm^3\ g^{-1}$ calculated at P/P_0 0.4, matching well with the calculated surface area and pore volume of 330 $m^2\ g^{-1}$ and 0.16 $cm^3\ g^{-1}$, respectively. Pore size distribution (PSD) calculated from N_2@77 K data revealed an average pore size of ~6 Å, which corroborates the simulated crystal structure. This confirms the successful conversion of the MXene into a porous MOF structure. Notably, although these values are lower than the theoretical maximum for defect-free MIL-71 analogs, the similarity in specific surface area between the bulk and nanosheet samples confirms that any subsequent behavioral enhancement in the nanosheet-based MOFs is driven mainly by morphological factors rather than a disparity in internal microporosity.

The UV-vis spectrum of the V_2CT_x–A MOF (Fig. S7) shows broad absorption starting near 500 nm with a maximum at approximately 400 nm, indicating strong light absorption in the visible region. The fluorescence spectra show a broader band with a slight blueshift in the emission band associated with the ADBA linker after the MOF is formed (Fig. 1c). High-resolution SEM images (Fig. 1d, e, and S8) revealed distinct morphologies: the MXene-derived MOF exhibited a petal-like 2D nanosheet structure, whereas the $VOSO_4$–A MOF formed rod-like crystals. One of the key advantages of MXene-derived MOFs is that the morphology of the precursor is largely preserved during MOF formation, enabling the controlled synthesis of 2D frameworks. Later TEM analysis (Fig. S9) reveals that the material consists of smaller nanosheets with an average size of ~20–40 nm. The low-magnification image shows aggregates of MOF nanosheets uniformly distributed, suggesting the controllable morphology. Furthermore, the images reveal the existence of crystalline MOF layers with a spacing of about 1.8 nm that corresponds to the simulated MOF structure, and not bulk MXene layers. In addition, the survey spectra and V 2p XPS spectra (Fig. S10) confirm the presence of one type of V^{5+} species associated with V_2CT_x–A MOF formed, and not with pristine V_2CT_x. Additionally, O 1s is shifted towards higher bonding energy corresponding to carboxylic oxygens, and the C 1s spectra showed that the bonds of MXenes (V–C) have disappeared, while aromatic C=C and C–O bonds originating from the anthracene ligands became dominant indicating that the MXene is completely consumed during MOF formation.

This approach provides insight into the influence of MXene morphology on MOF growth, a feature that conventional MOF synthesis typically lacks. The atomically thin MXene layers offer abundant reactive surface sites for the coordination of protonated ligands, facilitating framework assembly while maintaining the underlying 2D architecture.[32]

Sensing application

To investigate the influence of the MOF structure and morphology on sensing performance, the photoluminescence (PL) responses of the synthesized vanadium-based MOFs were evaluated toward a variety of cations, anions, and nitroaromatic compounds. In the case of cation sensing (Cu^{2+}, Pb^{2+}, Cd^{2+}, Fe^{2+}, Cr^{3+}, and Fe^{3+}), the $VOSO_4$–A MOF exhibited a general PL quenching effect upon exposure to all tested metal ions, consistent with previously reported behavior for anthracene-based Zr-MOFs.[42] However, significantly stronger quenching was observed primarily for Pb^{2+} and Fe^{3+} (Fig. 2a and b).

As shown in Fig. 2c and S11, the emission intensity decreased progressively with increasing concentrations of Fe^{3+} and Pb^{2+}. The corresponding Stern–Volmer (SV) plots (Fig. 2d and S12) revealed quasi-linear relationships within the tested concentration ranges, suggesting a dynamic quenching process. The Stern–Volmer constants (K_{SV}) were calculated to be 7.04 ×

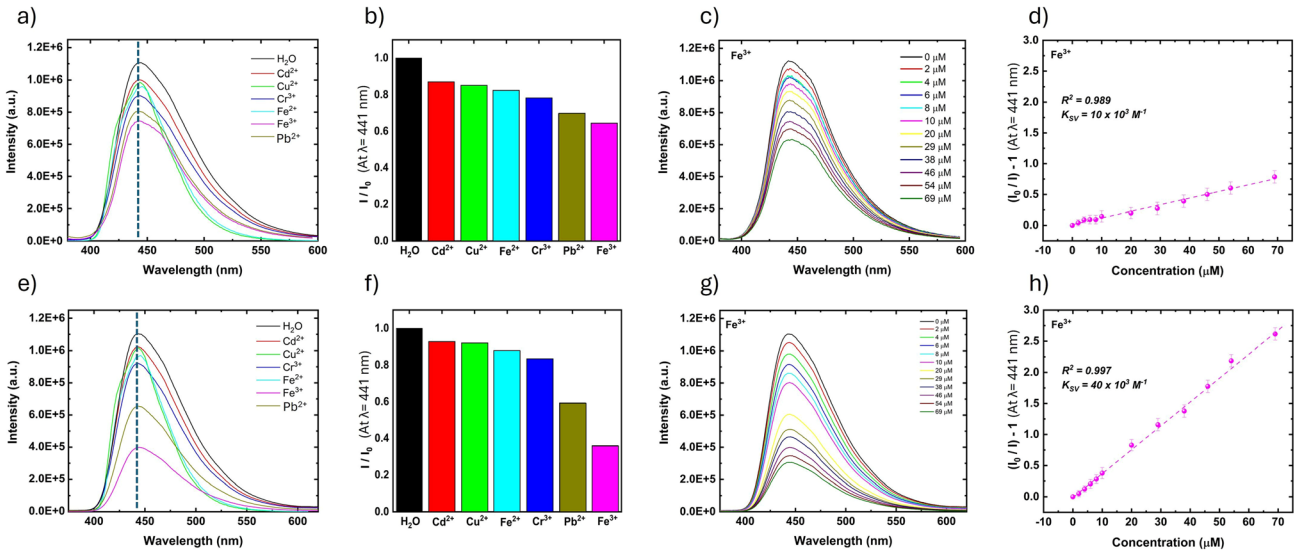

Fig. 2 (a) PL response of $VOSO_4$–A MOF toward metal cations. (b) Relative luminescence intensity of $VOSO_4$–A MOF suspensions toward metal cations. (c) Fluorescence-quenching titrations using Fe^{3+} for $VOSO_4$–A MOF. (d) SV plot of $[(I_0/I) - 1]$ *vs.* the concentration of Fe^{3+}. (e) PL response of V_2CT_x–A MOF toward metal cations. (f) Relative luminescence intensity of V_2CT_x–A MOF suspensions toward metal cations. (g) Fluorescence-quenching titrations using Fe^{3+} for V_2CT_x–A MOF. (h) SV plot of $[(I_0/I) - 1]$ *vs.* the concentration of Fe^{3+}.

10^3 M^{-1} for Pb^{2+} and 1.0×10^4 M^{-1} for Fe^{3+}, which are notably higher than those reported for UiO-68-AN-fcu and UiO-68-AN-hcp Zr-MOFs.[42] The limits of detection (LODs) were determined to be 323.6 μM and 2.63 μM for Pb^{2+} and Fe^{3+}, respectively.

To assess the effect of morphology, similar measurements were performed using the V_2CT_x–A MOF nanosheets. These nanosheets exhibited comparable selectivity but significantly enhanced sensitivity toward Pb^{2+} and Fe^{3+} (Fig. 2e–h). For Pb^{2+}, the SV plot remained quasi-linear up to 20 μM before reaching a plateau, indicating saturation of the available interaction sites (Fig. S12). The K_{SV} in the linear region was determined to be 4.63×10^4 M^{-1}, approximately six times higher than that of the bulk MOF. For Fe^{3+}, the SV plot remained linear over the tested concentration range, yielding a K_{SV} value of 4.0×10^4 M^{-1}, corresponding to a fourfold enhancement relative to the bulk material. The limits of detection were calculated to be 57.0 μM and 0.66 μM for Pb^{2+} and Fe^{3+}, respectively.

To further evaluate the selectivity and robustness of the sensing response, competitive interference experiments were performed. A mixture containing competing metal ions (Cu^{2+}, Cd^{2+}, Cr^{3+}, and Fe^{2+}) at concentrations of 60 μM and 120 μM produced negligible fluorescence changes, indicating minimal interference with the intrinsic emission of the MOF (Fig. S13). Upon addition of Fe^{3+} to the same ion mixture, a pronounced fluorescence quenching response was observed that closely matched the quenching behavior obtained with Fe^{3+} alone. These results demonstrate that the V_2CT_x–A MOF nanosheets possess strong anti-interference capability and can selectively detect Fe^{3+} even in the presence of multiple coexisting metal ions.

To further evaluate the practical applicability of the sensor, spike-recovery experiments were conducted using tap water samples. The collected tap water was filtered prior to analysis and spiked with known concentrations of Fe^{3+} (2, 10, and 50 μM). The samples were then analyzed under the same sensing conditions used in the calibration experiments. The detected concentrations were 1.5, 10.3, and 49.9 μM, corresponding to recovery values of 75%, 103%, and 99.8%, respectively (Table 1). The lower recovery at the lowest concentration likely arises from matrix effects and trace iron already present in the tap water sample. These results indicate that the V_2CT_x–A MOF sensor can reliably detect Fe^{3+} in real water matrices with good analytical accuracy, particularly at moderate and higher concentrations.

In anion sensing (HCO_3^-, HSO_3^-, $Cr_2O_7^{2-}$, $S_2O_3^{2-}$, and SO_3^{2-}), the V-MOF displayed a weak PL "turn-on" response in the presence of $Cr_2O_7^{2-}$, in contrast to the strong quenching observed for Zr–anthracene MOFs under similar conditions (Fig. 3a–d).[42] The reciprocal Stern–Volmer plot revealed a quasi-linear relationship within the tested concentration range, yielding a K_{SV} of 1.19×10^3 M^{-1} (Fig. 3d) and a LOD of 22.1 μM. Compared with the bulk MOF, the V_2CT_x–A nanosheets exhibited the same selectivity trend but with a slightly enhanced response (Fig. 3e–h), with a K_{SV} of 2.5×10^3 M^{-1} (Fig. 3h) and a LOD of 10.9 μM.

For nitroaromatic compounds (nitrobenzene, dinitrophenol, nitrotoluene, and dinitrotoluene), both MOFs exhibited fluorescence quenching toward all analytes; however, only nitrobenzene induced a significant response (Fig. 4a and b). The PL intensity decreased sharply with increasing nitrobenzene concentration, whereas negligible changes were observed for the other compounds (Fig. 4c and d). This contrasts with Zr–anthracene MOFs, which exhibit minimal response toward nitrobenzene but pronounced sensitivity toward dinitrophenol.[42] The V_2CT_x–A nanosheets displayed a similar selectivity pattern but with higher quenching efficiency, confirming the beneficial effect of nanosheet morphology in enhancing analyte accessibility and response intensity (Fig. 4e and f).

Further analysis of the detection limits using the equation $LOD = 3\sigma/K_{SV}$ (where σ is the standard deviation of the blank signal) revealed that the detection limits of $VOSO_4$–A MOF for Fe^{3+}, $Cr_2O_7^{2-}$, and nitrobenzene are 2.63, 22.09, and 1.27 μM, respectively, which are comparable to those of previously reported systems.[42,47–53] By comparison, the detection limits of V_2CT_x–A MOF for Fe^{3+}, $Cr_2O_7^{2-}$, and nitrobenzene are 0.66, 10.91, and 1.05 μM, respectively, demonstrating the enhancement effect associated with nanosheet morphology.

The improved sensing performance toward Fe^{3+}, Pb^{2+}, $Cr_2O_7^{2-}$, and nitrobenzene compared with Zr-based analogues is likely related to the distinct V-MOF framework topology, which affords a higher packing density and a more favorable orientation of anthracene linkers than the fcu and hcp analogues. Furthermore, the enhanced response of the nanosheets relative to the bulk MOF can be attributed to their morphology, which provides greater surface accessibility and facilitates faster diffusion of analyte species to the framework's active sites. The reduced diffusion path length maximizes the exposure of surface-active anthracene moieties and minimizes the pore-blocking limitations often encountered in bulk crystallites.

Table 1 The spike-recovery experiment using tap water and different concentrations of Fe^{3+} cations

Sample	Added (μM)	Found (μM)	Recovery
Tap water	2	1.5	75%
Tap water	10	10.3	103%
Tap water	50	49.9	99.8%

Sensing mechanisms

To understand the sensing mechanism, the influence of incorporating the ADBA linker into the MOF framework was first examined. Density functional theory (DFT) calculations were performed to analyze the electronic distribution in both the ground and excited states of the framework (Fig. S15 and S16). The results indicate that upon excitation, electron density partially shifts from the anthracene linker toward the vanadium metal centers. This redistribution is consistent with an internal ligand-to-metal charge transfer (LMCT) contribution within the framework and explains the slight spectral shift and broadening

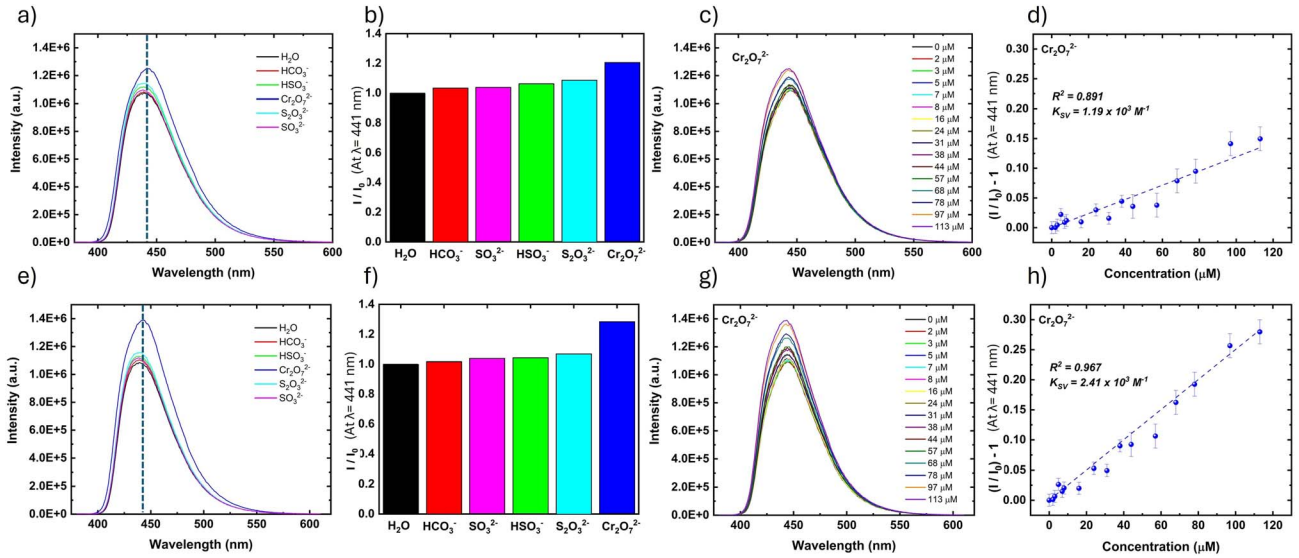

Fig. 3 (a) PL response of $VOSO_4$–A MOF toward anions. (b) Relative luminescence intensity of $VOSO_4$–A MOF suspensions toward anions. (c) Fluorescence-quenching titrations using $Cr_2O_7^{2-}$ for $VOSO_4$–A MOF. (d) SV plot of $[(I_0/I) - 1]$ *vs.* the concentration of $Cr_2O_7^{2-}$. (e) PL response of V_2CT_x–A MOF toward anions. (f) Relative luminescence intensity of V_2CT_x–A MOF suspensions toward anions. (g) Fluorescence-quenching titrations using $Cr_2O_7^{2-}$ for V_2CT_x–A MOF. (h) SV plot of $[(I_0/I) - 1]$ *vs.* the concentration of $Cr_2O_7^{2-}$.

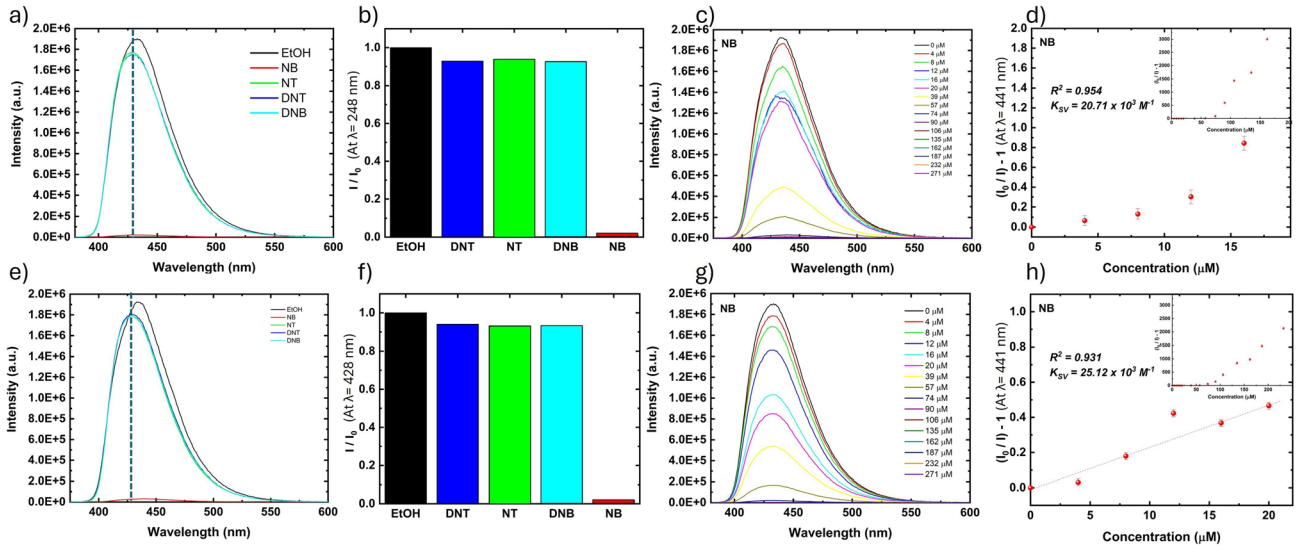

Fig. 4 (a) PL response of $VOSO_4$–A MOF toward nitro aromatics. (b) Relative luminescence intensity of $VOSO_4$–A MOF suspensions toward nitro aromatics. (c) Fluorescence-quenching titrations using NB for $VOSO_4$–A MOF. (d) SV plot of $[(I_0/I) - 1]$ *vs.* the concentration of NB. (e) PL response of V_2CT_x–A MOF toward nitro aromatics. (f) Relative luminescence intensity of V_2CT_x–A MOF suspensions toward nitro aromatics. (g) Fluorescence-quenching titrations using NB for V_2CT_x–A MOF. (h) SV plot of $[(I_0/I) - 1]$ *vs.* the concentration of NB.

observed in the photoluminescence (PL) spectrum of the MOF compared with the free ADBA linker. This LMCT process describes the intrinsic excited-state electronic structure of the MOF and does not directly represent the sensing mechanism.

To clarify how Fe^{3+} and Pb^{2+} affect the MOF emission, possible fluorescence quenching pathways were examined. The framework contains π-conjugated anthracene ligands that are highly sensitive to external electronic perturbations. Stern–Volmer plots for both Fe^{3+} and Pb^{2+} display high linearity (Fig. 2d and h), indicating that fluorescence attenuation follows a dynamic quenching process. Time-resolved photoluminescence measurements (Fig.s S17–S20) show only minor changes in fluorescence lifetime, decreasing from 5.17 ns for the pristine MOF to 4.91 ns in the presence of Fe^{3+} and 4.83 ns for Pb^{2+}. These small variations are consistent with dynamic quenching involving excited-state interactions between the fluorophore and analyte species.[42]

The quantum yield obtained (Fig. S21) from PLQY obtained is 73%. Density functional theory calculations were also carried out to identify the preferred interaction sites of the metal ions

within the framework. The optimized adsorption geometries obtained from DFT calculations are shown in Fig. S22–S24. The optimized structures indicate that both Fe^{3+} and Pb^{2+} adsorb near the vanadium-based metal cluster rather than forming direct coordination bonds with the organic linker. The calculated ion-cluster distances are approximately 3.4 Å for Fe^{3+} and 3.8 Å for Pb^{2+}, suggesting outer-sphere adsorption near the metal node. The corresponding binding energies are −11.9 eV for Fe^{3+} and −3.7 eV for Pb^{2+}, revealing significantly stronger interaction between Fe^{3+} and the MOF surface. Such interactions facilitate electronic coupling between the adsorbed ion and the excited anthracene linker, enabling photoinduced electron transfer (PET) from the excited linker to the electron-deficient analyte species, which leads to fluorescence quenching.

In addition to electron-transfer processes, resonance energy transfer may also contribute to the observed fluorescence attenuation. The emission spectrum of the MOF partially overlaps with the absorption bands of Fe^{3+} and Pb^{2+} (Fig. S16). Quantitative analysis of the spectral overlap yielded a spectral overlap integral of $J(\lambda) = 7.85 \times 10^{12}\ M^{-1}\ cm^{-1}\ nm^4$. Using standard Förster parameters ($\kappa^2 = 2/3$, $n = 1.33$, and $\Phi_D = 0.73$), the corresponding Förster distance (R_0) was estimated to be approximately 2–3 nm. This distance is comparable to the scale of surface interactions between the MOF linker and adsorbed ions, indicating that Förster resonance energy transfer (FRET) is geometrically feasible. However, the moderate magnitude of the spectral overlap suggests that FRET contributes only partially to the overall fluorescence quenching process.

A similar photophysical pathway can also explain the quenching behavior observed for nitroaromatic compounds. Nitroaromatic molecules are well-known electron acceptors because the strongly electron-withdrawing nitro group lowers the energy of the LUMO level, enabling efficient photoinduced electron transfer from excited aromatic fluorophores. In the present system, the excited anthracene linker can transfer electrons to nitroaromatic analytes that approach the MOF surface, resulting in fluorescence attenuation. Among the tested compounds, nitrobenzene exhibits the most pronounced quenching response. This behavior likely arises from favorable electronic coupling and spectral overlap between the MOF emission and the absorption spectrum of nitrobenzene. In contrast, more substituted nitroaromatics such as dinitrophenol or dinitrotoluene are sterically bulkier and interact less efficiently with the MOF surface, leading to weaker effective quenching under the present experimental conditions.

Adsorption experiments further support a surface-dominated sensing mechanism. Both V_2CT_x-MOF nanosheets and $VOSO_4$-MOF bulk samples exhibited negligible uptake of Fe^{3+}, nitrobenzene, and other tested analytes, indicating that the interaction occurs primarily at the external surface rather than within the internal pores. To evaluate the structural stability of the material under aqueous conditions (Fig. S14) the MOF sample was immersed in water for an extended period and subsequently characterized. The PXRD patterns (Fig. S14a) recorded before and after water exposure show no significant changes in the diffraction peaks, indicating that the crystalline structure of the material remains intact. The diffraction patterns of V_2CT_x–A MOF before and after water exposure show that the major characteristic peaks are largely preserved, suggesting good structural stability. Furthermore, the reusability of the fluorescence sensor was examined through repeated sensing cycles. After the sensing experiment, the material was recovered, washed with solvents, and tested by PXRD.[42]

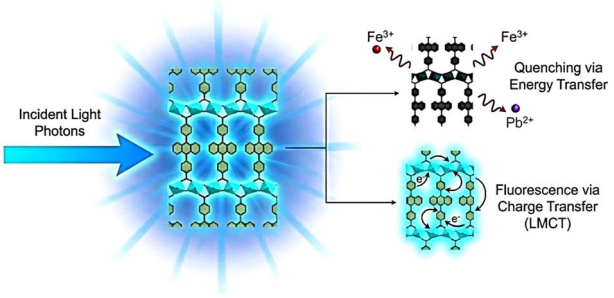

Fig. 5 Schematic representation of the quenching mechanism and the charge transfer mechanism.

Taken together, these results indicate that fluorescence quenching in the V-MOF arises mainly from dynamic interactions between the excited anthracene linker and analytes adsorbed near the framework surface. The intrinsic photophysics of the MOF involves partial LMCT character within the framework, whereas the sensing response toward external analytes is dominated by photoinduced electron transfer (PET), with a secondary contribution from resonance energy transfer enabled by spectral overlap between the MOF emission and analyte absorption (Fig. 5). The stronger adsorption and electronic coupling observed for Fe^{3+}, together with the strong electron-accepting character of nitrobenzene, account for their relatively higher quenching efficiencies in the sensing experiments.[42]

Conclusions

Anthracene-functionalized vanadium MOFs with various morphologies were successfully synthesized using $VOSO_4$ and V_2C MXenes as metal precursors. The resulting MOFs, $VOSO_4$–A (bulk) and V_2CT_x–A (nanosheet), demonstrate strong fluorescence properties and high selectivity toward Fe^{3+} and Pb^{2+} ions. Notably, the nanosheet morphology exhibited superior sensitivity because of its enhanced surface accessibility and shorter ion–diffusion pathways. Compared with previously reported Zr–anthracene MOFs, the sensing enhancement is attributed to the redox versatility of the vanadium framework and the improved distribution of organic linkers within the 2D topology. Spectroscopic studies and DFT analysis revealed that fluorescence quenching arises from a synergistic combination of dynamic processes involving LMCT driven by electron transfer from anthracene ligands to vanadium centers, as well as analyte-induced energy transfer. Ultimately, this work establishes a versatile 'top-down' synthetic paradigm that transcends simple structure replication, offering a robust strategy to

engineer morphology-dependent physicochemical properties in MOFs; this not only advances the specific domain of optical sensing but also paves the way for the next generation of MXene-derived architectures in energy conversion and environmental remediation. These findings underline the importance of structural morphology control in MOF-based sensor design and provide a foundation for developing next-generation, morphology-engineered MOFs for efficient optical monitoring of heavy metal contaminants in environmental systems.

Conflicts of interest

There are no conflicts to declare.

Data availability

The data that support the findings of this work are available from the corresponding author upon reasonable request. The data supporting this article have been included as part of the supplementary information (SI). Supplementary information: figures and tables; experimental procedures; material characterization; and sensing measurements. See DOI: https://doi.org/10.1039/d6ta00156d.

Acknowledgements

This work was financially supported by King Abdullah University of Science and Technology (KAUST) under Award No. URF/1/5066-01-01. We would like also to thank Dr Nimer Wehbe and Prof. Yoji Kobayashi for their help with this work.

Notes and references

1 M. Y. Tsang, A. Sinelshchikova, O. Zaremba, F. Schöfbeck, A. D. Balsa, M. R. Reithofer, S. Wuttke and J. M. Chin, *Adv. Funct. Mater.*, 2024, **34**, 2308376.
2 H. He, Y. Song, F. Sun, Z. Bian, L. Gao and G. Zhu, *J. Mater. Chem. A*, 2015, **3**(32), 16598–16603.
3 N. C. Burtch, J. Heinen, T. D. Bennett, D. Dubbeldam and M. D. Allendorf, *Adv. Mater.*, 2018, **30**, 1704124.
4 L. Kong, R. Zou, W. Bi, R. Zhong, W. Mu, J. Liu, R. P. S. Han and R. Zou, *J. Mater. Chem. A*, 2014, **2**, 17771.
5 A. Diaz-Marquez, S. Naskar, D. Fan, M. Eddaoudi and G. Maurin, *Chem. Sci.*, 2025, **16**, 19519–19531.
6 S. Mirzaei, M.-Y. Gao, A. H. Alawadhi, H. L. Nguyen, Z. Zhou, V. Singh, D. D. Ahn, D. M. Proserpio, M. O'Keeffe and O. M. Yaghi, *Chem*, 2026, **12**(2), 102830.
7 A. Ozcan, D. Fan, S. J. Datta, A. Diaz-Marquez, R. Semino, Y. Cheng, B. Joarder, M. Eddaoudi and G. Maurin, *Sci. Adv.*, 2024, **10**, 5846.
8 Y.-S. Xue, Y. He, L. Zhou, F.-J. Chen, Y. Xu, H.-B. Du, X.-Z. You and B. Chen, *J. Mater. Chem. A*, 2013, **1**, 4525.
9 Y. Cheng, S. J. Datta, S. Zhou, J. Jia, O. Shekhah and M. Eddaoudi, *Chem. Soc. Rev.*, 2022, **51**, 8300–8350.
10 Z. Hao, X. Song, M. Zhu, X. Meng, S. Zhao, W. Yang, S. Song and H. Zhang, *J. Mater. Chem. A*, 2013, **1**, 11043.
11 Q. Liu, L. Xie, X. Shi, G. Du, A. M. Asiri, Y. Luo and X. Sun, *Inorg. Chem. Front.*, 2018, **5**, 1570–1574.
12 J. Jia, F. Sun, H. Ma, L. Wang, K. Cai, Z. Bian, L. Gao and G. Zhu, *J. Mater. Chem. A*, 2013, **1**, 10112.
13 M. Shingole, S. Banerjee, B. Modak, S. Kolay, J. Mohanty and V. Sudarsan, *ChemPhotoChem*, 2025, **9**, e202400300.
14 M. Zeama, A. Alhaji, C. Serre, O. Shekhah and M. Eddaoudi, *Chem. Mater.*, 2025, **37**, 6193–6202.
15 L. Sankhla and H. S. Kushwaha, *J. Electron. Mater.*, 2024, **53**, 1896–1902.
16 M. Zeama, J. Jia, S. Zhou, M. C. Faleiros, U. Yaqoob, O. Shekhah, K. N. Salama and M. Eddaoudi, *Mat. Adv.*, 2024, **5**, 8432–8438.
17 X. Lu, K. Jayakumar, Y. Wen, A. Hojjati-Najafabadi, X. Duan and J. Xu, *Microchim. Acta*, 2023, **191**, 58.
18 H.-C. Zhou, J. R. Long and O. M. Yaghi, *Chem. Rev.*, 2012, **112**, 673–674.
19 Y.-M. Jo, Y. K. Jo, J.-H. Lee, H. W. Jang, I.-S. Hwang and D. J. Yoo, *Adv. Mater.*, 2023, **35**, 2206842.
20 J. Zhu, X. Chen, A. Q. Thang, F.-L. Li, D. Chen, H. Geng, X. Rui and Q. Yan, *SmartMat*, 2022, **3**, 384–416.
21 M. V. Nguyen, H. C. Dong, V. T. N. Truong, H. N. Nguyen, L. C. Luu, N. N. Dang and T. A. T. Nguyen, *New J. Chem.*, 2022, **46**, 632–641.
22 T.-Y. Dang, R.-H. Li, H.-R. Tian, Q. Wang, Y. Lu and S.-X. Liu, *Inorg. Chem. Front.*, 2021, **8**, 4367–4375.
23 F. Carson, J. Su, A. E. Platero-Prats, W. Wan, Y. Yun, L. Samain and X. Zou, *Cryst. Growth Des.*, 2013, **13**, 5036–5044.
24 A. Centrone, T. Harada, S. Speakman and T. A. Hatton, *Small*, 2010, **6**, 1598–1602.
25 J.-L. Zhang, Q.-X. Zhao, M.-Y. Cheng, W.-M. Xuan and Y. Liu, *Tungsten*, 2023, **5**, 261–269.
26 M. Zhu, X. Bai, S. Wang, Y. Yang, A. Zhang, J. Yang, Y. Lu, B. Li and S. Liu, *J. Alloys Compd.*, 2025, **1022**, 179861.
27 Z. U. D. Babar, V. Iannotti, G. Rosati, A. Zaheer, R. Velotta, B. Della Ventura, R. Álvarez-Diduk and A. Merkoçi, *Chem. Soc. Rev.*, 2025, **54**, 3387–3440.
28 M. Naguib, M. W. Barsoum and Y. Gogotsi, *Adv. Mater.*, 2021, **33**, 2103393.
29 A. Lakmal, P. B. Thombre and C. E. Shuck, *Acc. Chem. Res.*, 2024, **57**, 3007–3019.
30 M. Mustakeem, J. K. El-Demellawi, M. Obaid, F. Ming, H. N. Alshareef and N. Ghaffour, *ACS Appl. Mater. Interfaces*, 2022, **14**, 5265–5274.
31 Y.-Z. Zhang, Y. Wang, Q. Jiang, J. K. El-Demellawi, H. Kim and H. N. Alshareef, *Adv. Mater.*, 2020, **32**, 1908486.
32 H. Wu, M. Almalki, X. Xu, Y. Lei, F. Ming, A. Mallick, V. Roddatis, S. Lopatin, O. Shekhah, M. Eddaoudi and H. N. Alshareef, *J. Am. Chem. Soc.*, 2019, **141**, 20037–20042.
33 X. Ren, Y. Chen, L. Guo, Z. She, M. Gao, Y. Zhao and M. Shao, *Ecotoxicol. Environ. Saf.*, 2018, **164**, 1–11.
34 E. S. Henle, Y. Luo and S. Linn, *Biochemistry*, 1996, **35**, 12212–12219.
35 Y. Zhang, Y. Wang, R. Yu, S. Zhang and Z. Wu, *Front. Biol. China*, 2008, **3**, 50–54.

36 R. N. Jackson, D. Baird and S. Els, *Water SA*, 2005, **31**, 107–116.
37 M. Kirberger, H. C. Wong, J. Jiang and J. J. Yang, *J. Inorg. Biochem.*, 2013, **125**, 40–49.
38 B. Bansod, T. Kumar, R. Thakur, S. Rana and I. Singh, *Biosens. Bioelectron.*, 2017, **94**, 443–455.
39 L. A. Malik, A. Bashir, A. Qureashi and A. H. Pandith, *Environ. Chem. Lett.*, 2019, **17**, 1495–1521.
40 L. Fabbrizzi, M. Licchelli, P. Pallavicini, A. Perotti and D. Sacchi, *Angew. Chem., Int. Ed.*, 1994, **33**, 1975–1977.
41 N. Yadav, K. Kumar, S. Lakhera, V. Ragavendran, I. K. Pandey, U. N. Tripathi, S. R. Pathak and G. K. Rao, *J. Mol. Struct.*, 2026, **1350**, 143901.
42 D. Chen, T. Lu, Y. Chen and L. Yang, *Spectrochim. Acta, Part A Mol. Biomol. Spectrosc.*, 2023, **300**, 122916.
43 N. Kabeer, Y. Khan, M. Zeama, J. K. El-Demellawi, A. Justin, S. Kandambeth, V. S. Kale, O. Shekhah, H. N. Alshareef and M. Eddaoudi, *J. Mater. Chem. A*, 2025, **13**(47), 40919–40929.
44 M. Naguib, R. R. Unocic, B. L. Armstrong and J. Nanda, *Dalton Trans.*, 2015, **44**, 9353–9358.
45 A. Fateeva, P. Horcajada, T. Devic, C. Serre, J. Marrot, J.-M. Grenèche, M. Morcrette, J.-M. Tarascon, G. Maurin and G. Férey, *Eur. J. Inorg. Chem.*, 2010, **2010**, 3789–3794.
46 K. Barthelet, K. Adil, F. Millange, C. Serre, D. Riou and G. Férey, *J. Mater. Chem.*, 2003, **13**, 2208–2212.
47 Z.-t. Shang, T.-m. Li, J.-h. Han, F. Yu and B. Li, *Inorg. Chim. Acta*, 2023, **550**, 121436.
48 Y. Liu, Y. Wang, Y. Zhang, P. G. Karmaker, L. Zhang, F. Huo, X. Yang and B. Zhao, *Dyes Pigm.*, 2022, **199**, 110099.
49 Z. Sun, J. Li, X. Wang, Z. Zhao, R. Lv, Q. Zhang, F. Wang and Y. Zhao, *J. Lumin.*, 2022, **241**, 118480.
50 X. Zhang, Q. Ma, X. Liu, H. Niu, L. Luo, R. Li and X. Feng, *Food Chem.*, 2022, **382**, 132379.
51 Y. Li, Z. Wei, Y. Zhang, Z. Guo, D. Chen, P. Jia, P. Chen and H. Xing, *ACS Sustain. Chem. Eng.*, 2019, **7**, 6196–6203.
52 X.-Y. Guo, Z.-P. Dong, F. Zhao, Z.-L. Liu and Y.-Q. Wang, *New J. Chem.*, 2019, **43**, 2353–2361.
53 B. Parmar, Y. Rachuri, K. K. Bisht, R. Laiya and E. Suresh, *Inorg. Chem.*, 2017, **56**, 2627–2638.

